JOURNAL OF APPLIED ELECTROCHEMISTRY **28** (1998) 141–150

On texture formation of chromium electrodeposits

C. BERGENSTOF NIELSEN*,‡, P. LEISNER§, A. HORSEWELL*

**Materials Research Department, Risø National Laboratory, DK-4000 Roskilde, Denmark*
Department of Physics‡ and Department of Manufacturing Engineering§, Technical University of Denmark,
DK-2800 Lyngby, Denmark

Received 5 February 1997; revised 27 June 1997

The microstructure, texture and hardness of electrodeposited hard, direct current (DC) chromium and pulsed reversed chromium has been investigated. These investigations suggest that the growth and texture of hard chromium is controlled by inhibition processes and reactions. Further, it has been established that codeposition of Cr_2O_3 nanoparticles is a general feature of DC chromium electrodeposition.

Keywords: *chromium*, *electrodeposition*, *texture formation*

1. Introduction

Electrodeposited hard chromium deposits are used in applications requiring hard, wear and corrosion resistant surface coatings. Various deposition parameters (effect of bath temperature, catalysts, current density on microstructure, morphology mechanical and corrosion properties) have been the subject of investigation by a number of researchers [1–8].

Different hypotheses have been put forward to explain the nature of chromium electrodeposition, [e.g. 4, 9]. It is widely assumed, following Snavely [9], that the large intrinsic tensile stresses in chromium deposits result from the deposition of an intermediate, metastable hydride that decomposes to metallic chromium and releases hydrogen. The associated volume change is thought to account for the residual stress in the deposit. However, such intermediate hydride formation was proposed on the basis of X-ray diffraction experiments on the surface of chromium deposits and has not been established by other techniques. It is also difficult to relate hydride formation to the effects of bath conditions (catalyst concentration, current density etc.). It should be emphasized that until now there is no experimental evidence (such as *in situ* X-ray diffraction of the deposition process) that shows that this process actually occurs.

One of the microstructural features of hard chromium electrodeposits is a strong <1 1 1> texture [7, 9]. Since the 1950s, a general theory on texture formation for electrodeposits has been developed. Considering that electrodeposits usually exhibit very large residual tensile stresses, earlier theories [10–12] suggested that the texture is a result of a cold work-like mechanism as seen in the plastic deformation that occurs during cold drawing of wires. In modern theories, texture formation is considered to arise from basic processes occurring during the electrochemical crystal growth process. As such we consider nucleation and growth of competing crystal surfaces. These processes may depend on the relative surface energies of the growing crystals or the effects may be influenced and under some conditions dominated by kinetic effects during deposition.

When electrodeposition is carried out in additive-free baths, at low current densities and high temperatures, the crystallites are often oriented with the most densely populated atom plane parallel to the substrate [13]. According to Finch's school [14, 15] the deposited metal then adopts the lateral type of growth with b.c.c. metals having a preferred orientation of <1 1 0>. If the deposition is carried out at low temperatures and high current densities, the crystallites of the deposits are oriented so that the most densely populated atom row, in the most densely populated atom plane, is perpendicular to the substrate. The deposited metal adopts an outward type of growth; with dominant <1 1 1> orientations (see [16]). There are, however, some implications in the understanding of texture as a result of either lateral or outward growth. First, the crystal directions of the deposited nuclei should have a near random distribution of all directions [13, 17, 18]. Second, the average distribution of crystal directions of the grown crystals should also be random, neither of which is not observed.

A series of conventional direct current (DC) electrodeposited chromium, where the plating temperature and current density have been the variable parameters, has been investigated. Also, a series of pulsed reversed (PR) electrodeposited chromium has been studied. The PR process is understood as being an electrodeposition with a cathodic pulse period and an anodic pulse period. For more details on equipment and procedures consult [7]. The hardness and crack density of these DC and PR chromium deposits have been found, see [7]. From this work, two samples have been chosen for further microstructural investigation, one DC chromium and one PR

0021-891X

chromium. The DC Cr that was chosen was the one with the highest crack density. It also had the highest Vickers hardness ($HV_{0.1}$ = 11 GPa) (see Fig. 5) The PR chromium chosen was the one which was deposited without microcracks (see Fig. 6) this specimen also had the lowest hardness of the series of PR Cr coatings ($HV_{0.1}$ = 5.5 GPa).

In this paper the microstructural observations of the two chromium electrodeposits will be considered with respect to the electrodeposition parameters used. The observations from this work are considered in the light of the hypothesis that the conventionally deposited DC chromium has a texture and a microstructure which is due to inhibition of certain crystal directions, and not a result of kinetic limitations caused by a high deposition rate as suggested by the outwards growth model.

2. Experimental details

2.1. *Electrochemical deposition*

The electrodeposits investigated were obtained from a conventional additive-free chromic acid bath. The bath contained 250 g dm^{-3} CrO_3, 2.5 g dm^{-3} H_2SO_4. The deposition was accomplished without stirring. 18/8 stainless steel substrates were pretreated in 50% H_2SO_4 and anodized at 10 A dm^{-2} for 90 s. The chromium was deposited onto the 18/8 stainless steel substrate until a layer of 25 μm was achieved. The DC chromium was deposited with a current density of 5000 A m^{-2} and a bath temperature of 50 °C. The current efficiency of the DC chromium was 16%. This type of plating bath is known to give bright, <1 1 1> textured hard coatings. The chromium coatings have been shown to contain microcracks [7, 8] (see also Fig. 6).

The PR chromium deposit was deposited with a pulsating current where the cathodic current density was 5000 A m^{-2} for 30 s and the anodic current density was 1500 A m^{-2} for 0.3 s. Hence the total anodic charge was 0.3% of the cathodic charge. The current efficiency of the PR Cr was 28%. The bath temperature of the PR chromium deposition experiment was 50 °C. The surface of the PR chromium deposit is not bright, but is free of microcracks [7, 8] (see also Fig. 6).

3. Microstructural observations

To understand the texture formation phenomenon of the chromium electrodeposits the microstructure was characterized with X-ray diffraction and cross sectional transmission electron microscopy (XTEM).

3.1. *X-ray experiments*

3.1.1. X-ray of DC chromium. Using a conventional X-ray diffractometer (STOE, Germany) operated in the 2Θ–Ω mode, it was found that the DC chromium deposit exhibits a strong <1 1 1> texture; (Fig. 1).

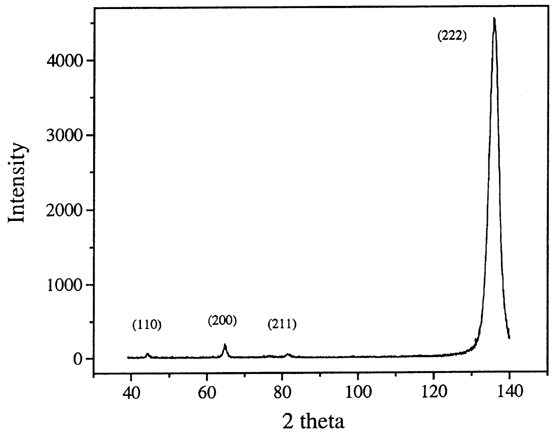

Fig. 1. 2Θ–Ω scan of the DC Cr.

The specimen was rotated about the normal to the plane of the surface coating during the measurement. The incident CuK_α radiation was from a copper X-ray tube operating at 40 kV and 30 mA. The total intensities of the peaks were obtained by integration allowing for intensity factor correction. This gives a distribution of the lowest index directions as follows; $\{1\,1\,1\} \sim 99\%$, $\{1\,1\,0\} < 1\%$, $\{2\,0\,0\} < 1\%$, $\{2\,1\,1\} < 1\%$ and $\{3\,1\,0\} < 1\%$.

XTEM suggested the presence of tiny oxide particles with {1 1 2} habit planes lying parallel with the $\{1\,1\,1\}_{Cr}$ planes. Since the low index diffracting planes of the oxide are therefore expected to be parallel to the plane of the substrate, it is necessary to perform the X-ray diffraction experiment at lower angles and with a higher counting time to be able to achieve sufficient intensity in the oxide peaks. The lattice parameter of the suspected Cr_2O_3 plane that was investigated is $d_{\{1\,1\,2\,0\}} = 248$ pm, which corresponds to 2Θ of 36°. The 2Θ scan was therefore performed from well below this value to establish if there was diffraction from other chromium oxide phases not indicated in XTEM. The 2Θ–Ω scan is shown in Fig. 2. The ordinate axis is chosen as logarithmic to enhance peaks of low intensity.

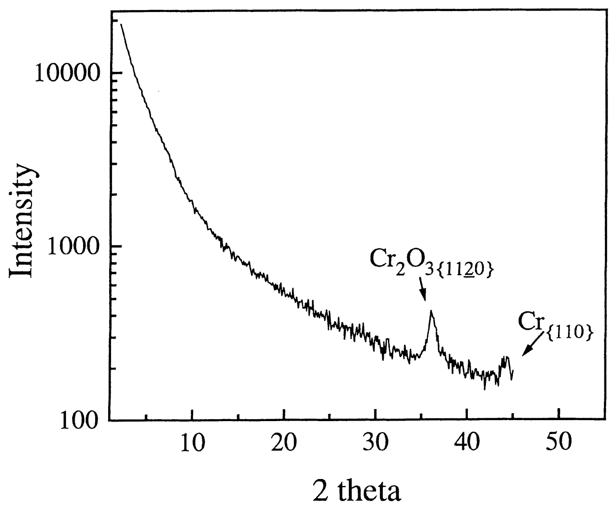

Fig. 2. 2Θ–Ω scan of the DC Cr at low angles.

The counting time and the collimation setup used gave a background intensity that was 60 times greater than the first diffraction experiment. A peak can be seen at the position expected for Cr_2O_3. The presence of this peak is taken to indicate that particles of chromium oxide are present in the electrodeposit. This was subsequently confirmed by XTEM below. No peaks from other crystal planes of the particles were obtained, which suggests a close orientation relationship between the highly textured chromium matrix and the codeposited oxide particles. Further, it was not possible to obtain peaks from other second phases that might possibly be expected. These second phases that were *not* found could, for example, be CrH or CrH_2.

3.1.2. X-ray of PR chromium. The X-ray diffraction experiment performed on the DC chromium has similarly been performed on the PR chromium. The results can be found in Figs 3 and 4. Figure 3 shows the diffractogram of the chromium reflections. Again the total intensities of the peaks were obtained by integration, allowing for intensity factor correction. This gives a distribution of the lowest index directions as follows; $\{1\,1\,1\} = 25\%$, $\{1\,1\,0\} = 20\%$, $\{2\,0\,0\} = 19\%$, $\{2\,1\,1\} = 18\%$ and $\{3\,1\,0\} = 17\%$. Hence, the distribution of crystal directions corresponds to the diffractogram from a powder diffraction sample and may be considered random. In Fig. 4 the result of the $2\Theta = 2°–40°$ diffraction experiment is shown. The only peak, is that resulting from diffraction by the $\{1\,1\,0\}$ planes of the chromium. Therefore, if there are oxides or hydrides present, they have a volume fraction of less than 1%, which renders them impossible to detect with X-ray diffraction.

3.1.3. Grain size estimation. The grain size of the PR and the DC chromium was determined. Using a standard powder sample of large grained chromium crystals (with grain sizes > 1 μm), the line broadening was divided into an instrumental peak broadening and a grain size/strain peak broadening, through deconvolution of the peaks. Using the Williamson–Hall plot, that evaluates the strain and grain size contributions to the peak broadening, the mean particle size of the DC chromium were found to be between 10 and 20 nm. The mean particle size of the PR chromium was found to be between 50 and 70 nm. There is a factor of 4.75 ± 2.25 between the grain sizes of the two electrodeposits, which explains the hardness difference according to the Hall–Petch relationship. Thus the hardness of polycrystalline metals follows the hardness/grain size relationship,

$$H = H_0 + kD^{-n} \tag{1}$$

where H is the hardness, H_0 is the hardness of very large grained material, k is a material constant, n is an exponent most often found to be equal to 0.5 and D the average grain size [20]. However, since the hardness of only two samples has been measured here, and the expression has three unknown parameters, it is difficult to say if the hardness difference is due to the grain size effect alone.

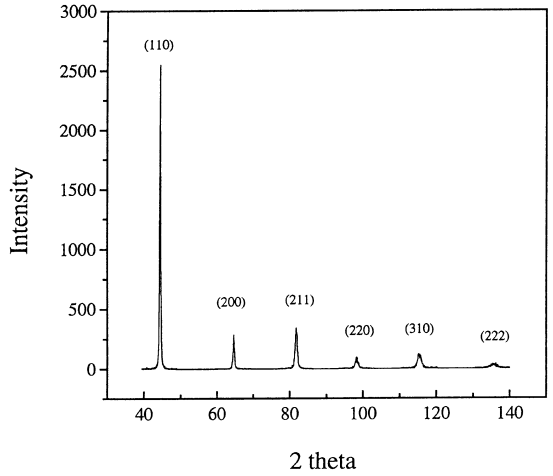

Fig. 3. 2Θ–Ω scan of the PR Cr.

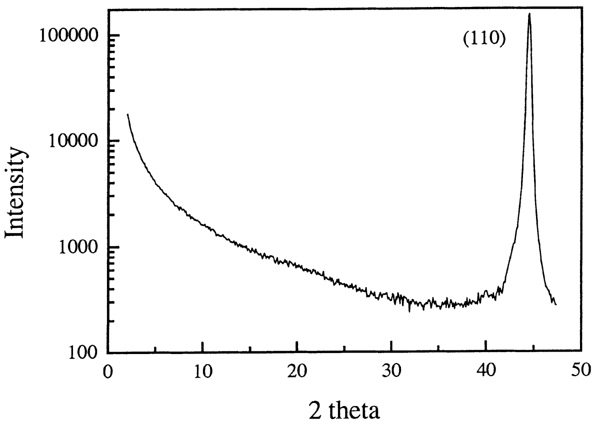

Fig. 4. 2Θ–Ω scan of the PR Cr at low angles.

3.2. *Scanning electron microscopy*

SEM micrographs of the DC Cr and the PR Cr are presented in Figs 5 and 6 in order to illustrate the difference in crack density in the two coatings. The samples were electropolished for a short time so that

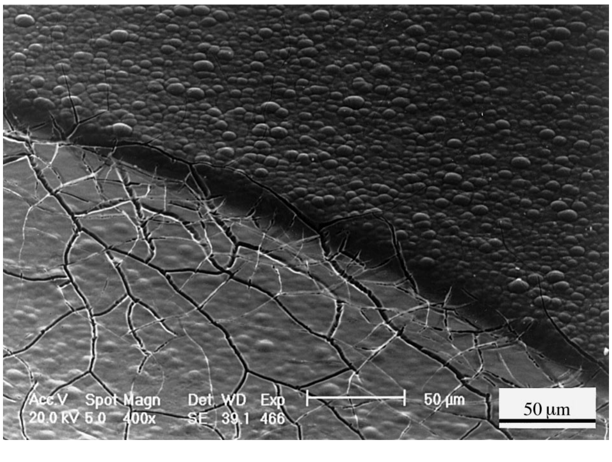

Fig. 5. SEM micrograph of the surface of the DC Cr. Upper right part of the micrograph is as-deposited Cr and lower left part of the micrograph shows the electropolished Cr surface with easily identified cracks.

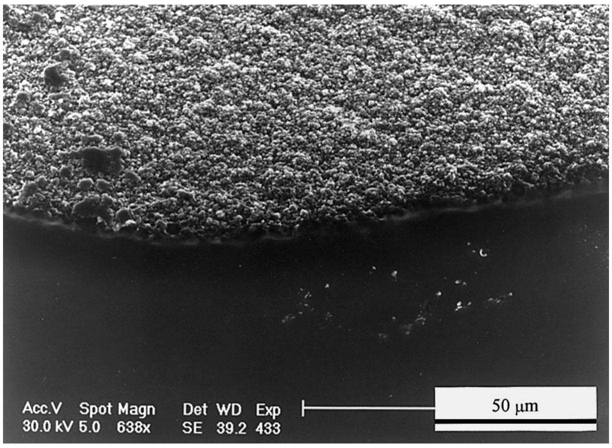

Fig. 6. SEM micrograph of the surface of the PR Cr. Upper part of the micrograph is as-deposited Cr and lower part of the micrograph shows the electropolished Cr surface. The electropolishing has removed the rough surface of the coating, but it has not revealed any cracks.

the cracks were easier to identify. The sample preparation is described in [8]. In the micrographs, both the as-deposited and the electropolished surface of the coatings are shown. In Fig. 5 it can be seen that the DC Cr surface has a high microcrack density. This crack pattern is typical for an isotropic material with a homogeneous equal biaxial tensile stress state and, therefore, resembles the crack pattern found in related systems, as for example in dried desert mud. In Fig. 6 it is seen that there are no micro cracks in the PR Cr coating surface. The as-deposited surface of the DC Cr is much more smooth than the as-deposited surface of the PR Cr. For this reason the two as-deposited coatings appear bright and dull, respectively.

3.3. *Cross-sectional transmission electron microscopy*

3.3.1. Sample preparation. To perform XTEM, a sample was cut and ground so that a cross-section of the substrate and the chromium deposit was less than 100 μm thick. The deposit was then electropolished in a perchloric acid–ethanol mixture using a modified window technique [21]. The penetration of the foil was situated at the substrate/deposit interface with electron transparent regions close to and up to 5 μm from the interface. Therefore, the XTEM investigations elucidate the part of the electrodeposit that corresponds both to the stable growth condition and the initial growth microstructure.

3.3.2. XTEM investigation. Cross-sectional TEM was performed on the DC chromium, since this was the most promising deposit seen in relation to features relating to the deposition parameters, i.e. it contained microcracks, a strong texture and the grain sizes were determined to be 10 to 20 nm.

The micrographs presented below will show the following features of the microstructure: Initial growth on the substrate/chromium interface, growth morphology, columnar or fibre shape of chromium crystals, height and width of the fibres, a highly dislocated microstructure of the grains, the typical orientation relationship between the grains, and presence of nanoprecipitates in the crystals.

3.3.3. Initial growth on the substrate. In Fig. 7, a bright field (BF) image of the steel substrate/chromium interface is shown. It can be seen that the growth, at least after 10 nm from the interface, has become columnar with grains growing perpendicular to the substrate. This is traditionally referred to as a field oriented texture. However, due to a too large foil thickness of the deposit, it is difficult to measure the height and width of the grains from this part of the sample. A typical column size is measured to 20 nm × 80 nm. Using the DF technique and by tilting and rotating the XTEM sample, it is seen that the initial grains have not grown epitaxially on the steel substrate.

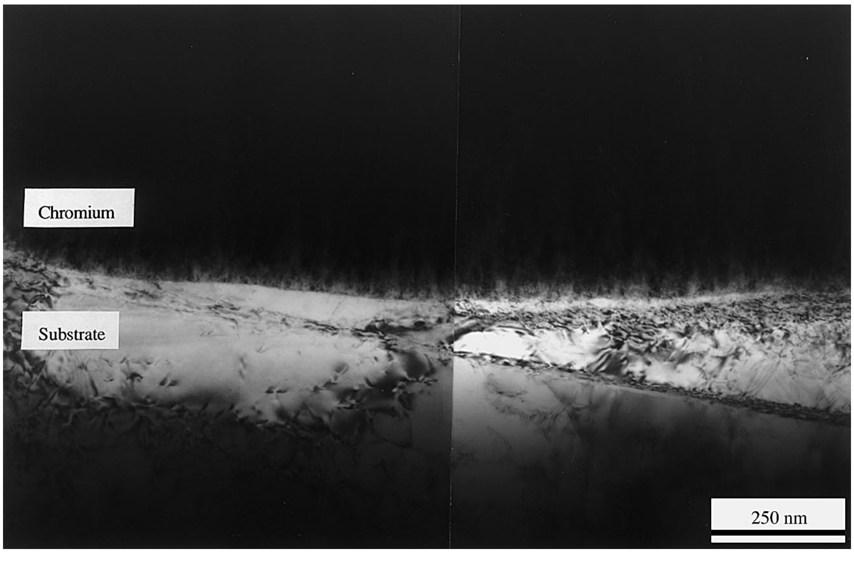

Fig. 7. BF image of the steel substrate/chromium interface.

3.3.4. Morphology. Figure 8 shows a BF image of the morphology of the chromium electrodeposit in the stable growth condition. The columnar grains initially grow perpendicular to the substrate as seen in Fig. 7. The substrate, however, is not ideally smooth, which causes the columns to grow out in a fan-shaped manner. The fan-shaped areas eventually meet and impinge as seen in Fig. 8. This kind of growth mechanism and impingement follows the Huygens principle known from geometric optics. Simply, consider a row of point shaped wave emitters, and let these emit circular shaped waves. Then, relatively close to the row of emitters, the noninterfered wave front will have a rough appearance. Further and further away from the row of wave emitters, the wave front becomes smoother and smoother since the curvature of each propagating wave gets smaller as the radius of the wave increases. In this way it can also be seen that small waves will eventually be overgrown by larger waves. Using this model [22, 23] it can be shown that if an initially rough interface grows with a constant velocity along the local surface normal, this leads to the formation of cusp singularities that decrease in number with time as the larger columns dominate the smaller ones. During this coarsening process, the interface becomes progressively smoother. Considering the small grain size of the chromium deposit (20 nm × 80 nm, which is smaller than the wavelength of light) this explain how chromium, when deposited with the right plating parameters, becomes bright, even when deposited on a rough substrate surface.

As the grains have the same outwards crystal orientation, i.e. <2 2 2>, the individual grains are extremely small and difficult to distinguish from each other in the micrographs.

3.3.5. Columnar growth and orientation of Cr crystals. Figure 9 shows an enlarged area of Fig. 8. Figure 9 is a BF image. Even at this high magnification, (160 K) it is difficult to distinguish the individual grains. The area marked by the four pointers is 75 nm wide and

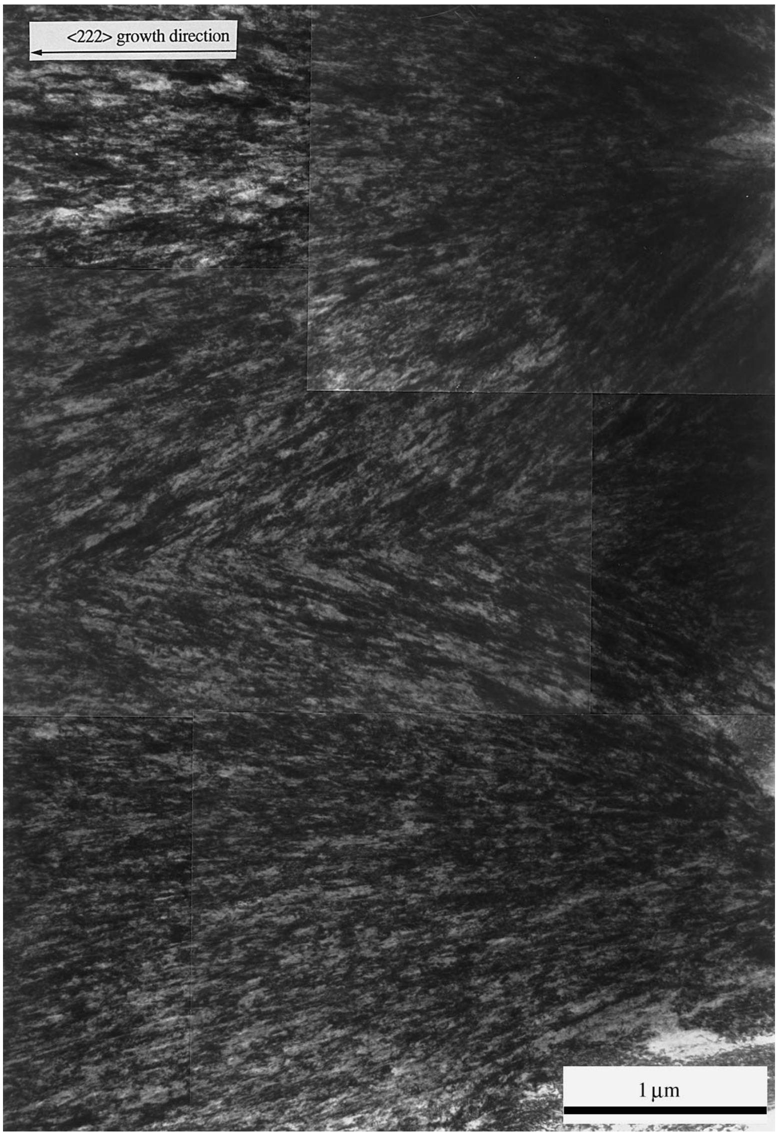

Fig. 8. BF image of the morphology of the chromium electrodeposit.

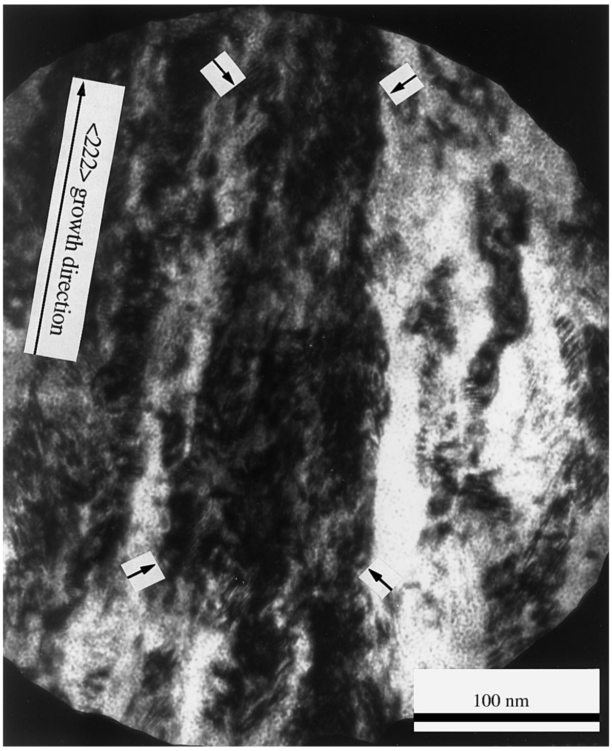

Fig. 9. Magnified part of the microstructure shown in Fig. 8.

375 nm long. Since this is a BF image, the dark area corresponds to one or more crystals that are strongly diffracting. It is not possible from such a BF image to accurately determine the number and size of crystals in the diffracting area of the sample. However, we may estimate that this area, with a size of about 30 nm × 150 nm, consists of four to eight grains, which is a constant grain size of the deposit in the stable growth zone. The structure is seen to be highly dislocated.

From the selected area diffraction patterns (SADPs) obtained from the microstructure, it is possible to determine the crystallographic orientation relationships between the electrodeposited chromium crystals. Figure 10 shows the SADP of the microstructure shown in Fig. 9. This SADP is typical for the microstructure of the DC Cr deposit.

Disregarding the diffraction from precipitates which will be treated below, the SADP in Fig. 10 can be explained as follows. Consider the grains to be arranged as suggested schematically in Figs 11 and 12, which show plan and cross sectional views, respectively. Let grain B be a twin crystal of grain A, with a {2 1 1} plane as mirror plane. Then, when the electron beam passes through the crystal pair A and B along the <0 1 1> zone axis, and at the same time through another crystal pair A and B along the <2 1 1> zone axis, then the resulting diffraction pattern will be as shown in Fig. 13, which corresponds to the SADP in Fig. 10. The SADP is therefore a result of diffraction from three crystal orientations with respect to the electron beam. The SADP in Fig. 10 is typical for the electrodeposit, so the orientation relationship between the columnar fibres, as shown in

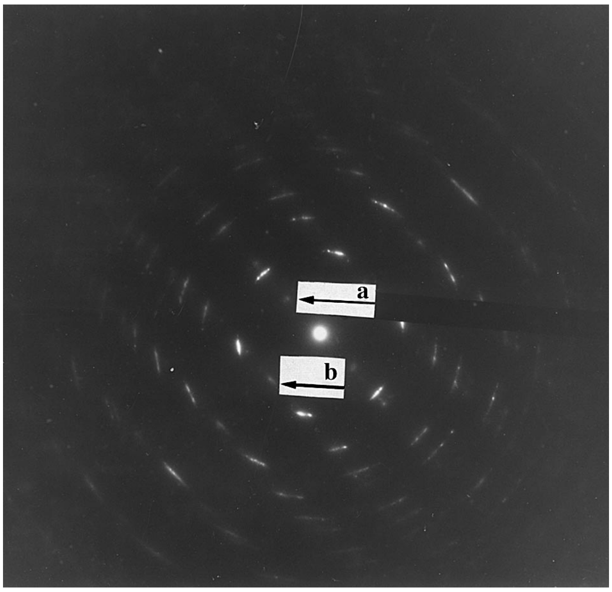

Fig. 10. The SADP of the area presented in Fig. 9.

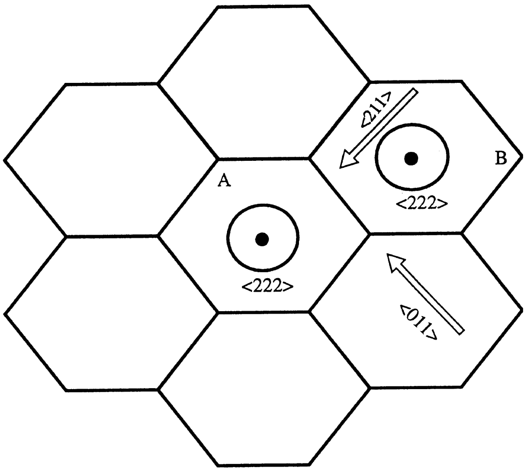

Fig. 11. The crystal arrangement shown from above.

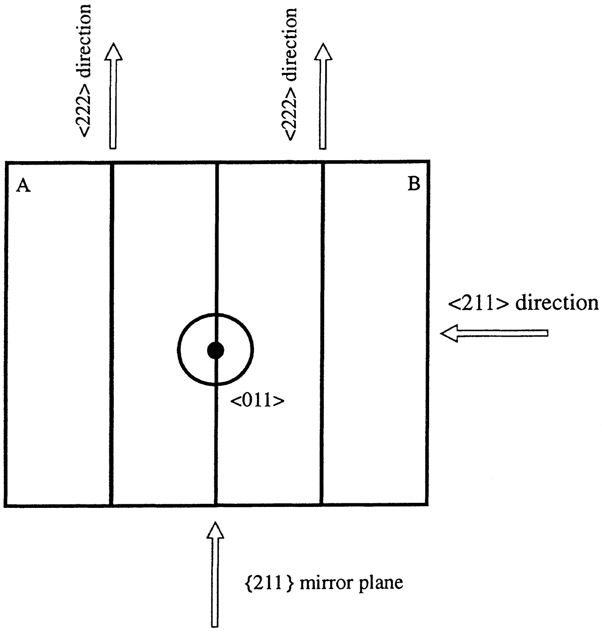

Fig. 12. The crystal arrangement shown from the side.

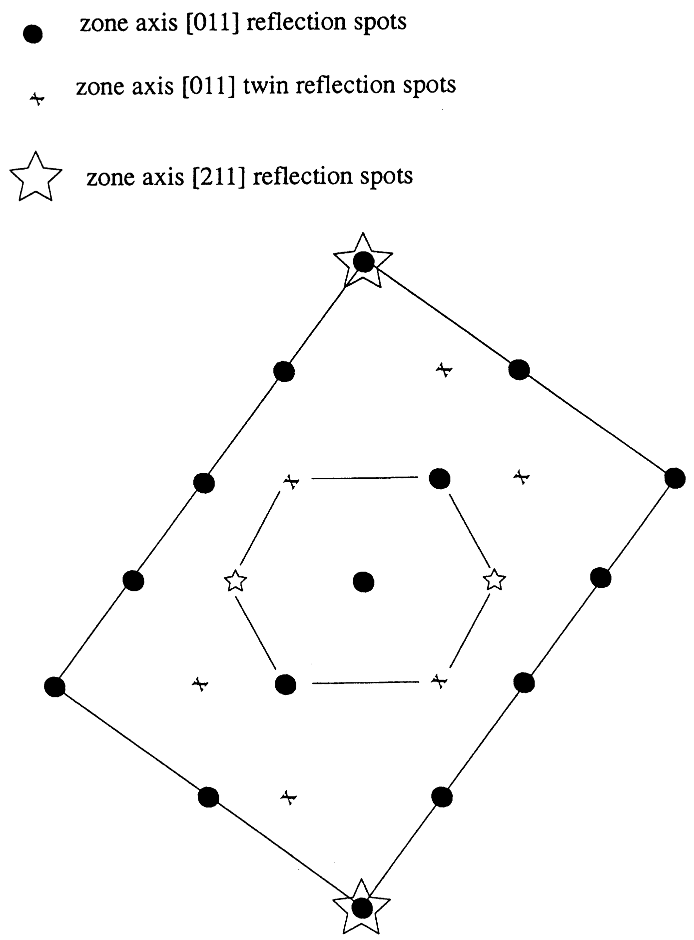

Fig. 13. Resulting SADP when electron beam passes through crystal pairs in the <0 1 1> direction and at the same time passes through other crystal pairs in the <2 1 1> direction.

Fig. 10, is a general feature of the microstructure. XTEM images show columnar crystals. However, the grain boundaries are curved, as shown in Fig. 9. The schematic drawing of the grains may therefore be understood as a description of the orientation relationships and not as a statement that the grain boundary planes are purely of the {2 1 1} type.

3.3.6. Precipitates; orientation, phase, shape and size. Using the dark field (DF) technique, it has been established that there are precipitates in the chromium deposit and hence the size, shape, phase and orientation relationship with the chromium matrix has been investigated. However, it has only been possible to obtain diffraction from the precipitates when there was strong diffraction from the {1 1 0} reflections of the chromium matrix.

In Fig. 10, the SADP from Fig. 9 is shown. The brightest spots in the diffraction pattern are recognised as {1 1 0} reflections of the chromium. Closer to the 0 0 0 spot, weaker spots can be seen. In Fig. 14, the DF image that resulted from the weak spot indicated by the pointer ‘a’ is shown. It can be seen from this precipitate dark field image that a large number of nanoparticles has been codeposited during growth on the chromium crystal. The finely dispersed nanoparticles are needle shaped, with the long side deposited along the chromium matrix crystal. The average size of the particles is about 1.5 nm × 6 nm. In Fig. 10, the diffraction spot indicated by pointer ‘b’ shows streaking due to the shape factor effect.

In Fig. 14 it is only within one column that the precipitates are visible, suggesting an epitaxial relationship with the chromium matrix. Based on the calculated *d*-spacings from the SADP in Fig. 10 (reflection spot ‘a’ and ‘b’) that gave $d \approx 248$ pm and $d \approx 364$ pm, with an angle between the two of 90°, the powder diffraction file was consulted to find a best match between chromium derivates (e.g. oxides, hydroxides, oxide–hydroxides, hydroxide–hydrates, sulphate–hydroxides) that could be expected to crystallize on the cathode during chromium electrodeposition. It was found that Cr_2O_3 (hexagonal with $a = 496$ pm and $c = 1359$ pm) fits the *d*-spacing and crystal plane criterion as it has $d_{\{1\,1\,\bar{2}\,0\}} = 248$ pm and $d_{\{\bar{1}\,1\,0\,2\}} = 363$ pm and the angle between the two crystal planes is 90°.

As seen in Fig. 10, $Cr_{\{2\,2\,2\}}$ is parallel with $d_{\{1\,1\,\bar{2}\,0\}}$ and $Cr_{\{1\,1\,0\}}$ is parallel with $d_{\{0\,1\,\bar{1}\,2\}}$. This orientation relationship is typical for the SADPs found. Further, it has only been possible to obtain diffraction from the Cr_2O_3 when there was strong diffraction of the {1 1 0} chromium planes. In Fig. 14, it is seen that the precipitates only can be seen in the strongly diffract-

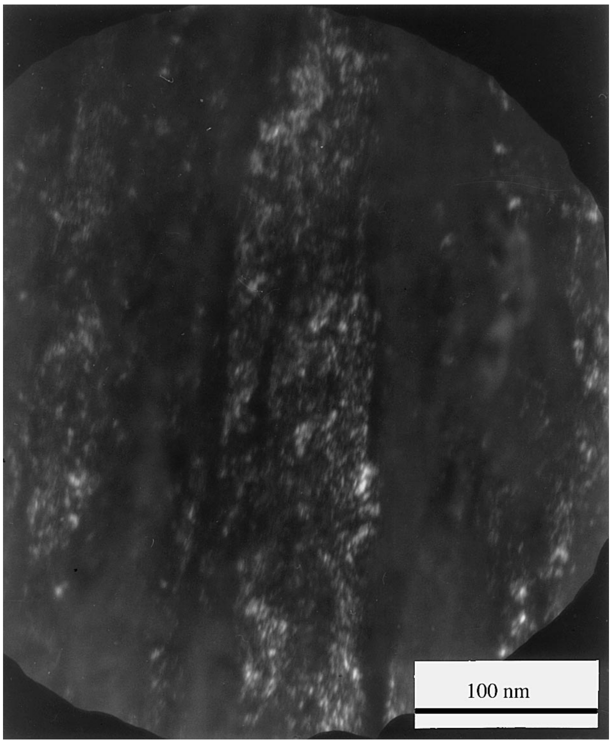

Fig. 14. DF image of the codeposited nanoparticles.

ing column, and not in the surrounding crystals. All these experimental results suggest that the chromium oxide grows epitaxially on the chromium matrix. Using a stereographic projection oriented with the chromium $\{1\,1\,1\}$ parallel with the $Cr_2O_{3\{1\,1\,\bar{2}\,0\}}$ plane and with the chromium plane $\{\bar{1}\;1\;0\}$ parallel with the $\{\bar{1}\;1\;0\;\bar{2}\}$ plane as dictated by the SADP in Fig. 10, then the $d_{\{\bar{1}\,1\,0\}} = d_{\{\bar{1}\,0\,1\}} = 204$ pm, and the $d_{\{\bar{2}\,2\,0\,\bar{4}\}} = d_{\{\bar{2}\,2\,0\,4\}} = 183$ pm. The angle between the two chromium planes is 60° and the angle between the two Cr_2O_3 planes is 64.6°. The *d*-spacing difference is below 11% mismatch. Consequently it is possible that the Cr_2O_3 crystallises with $\{1\;1\;\bar{2}\;0\}$ parallel to the $\{1\,1\,1\}$ chromium plane and with the $\{\bar{2}\;2\;0\;4\}$ planes of the Cr_2O_3 parallel with chromium $\{1\,1\,0\}$.

It is possible to estimate the volume fraction of the codeposited nanoparticles by measuring the projected area of these compared to the matrix images. The DF image in Fig. 14 represents the highest density observed and is therefore a worst case of codeposition of chromium oxide. The typical volume fraction of the nanoparticles is estimated from many such DF images to be approximately 5%.

4. Discussion

As shown both experimentally [18] and theoretically [17], the distribution of crystal directions of deposited nuclei should be random and, hence, that the final electrodeposit should also have a random distribution of crystal orientations. The development of texture may be explained by restrictions in crystal growth by codeposited species. In some cases the hypothesis of the presence of inhibiting species is supported by electrochemical impedance measurements [19]. In the case of electrodeposition of DC chromium it is also reasonable to consider the role of inhibiting species which in this case would be adsorbed hydrogen as it is codeposited in the electrochemical process. Furthermore, it is attractive to consider that DC Cr is textured as a result of inhibition by adsorbed hydrogen and that the PR Cr, that has very weak texture, has deposited with little or no inhibition due to the removal of hydrogen by the reverse pulse during plating. The comparison between DC and PR chromium will be divided in the following points; plating current efficiency, crystal orientations, grain size, hardness, microcrack density and codeposition of Cr_2O_3 nanoparticles.

4.1. *Current efficiency*

In the following there will be a discussion on the difference in degree of hydrogen codeposition in the case of DC and PR-deposited chromium. The experimental details can be found in [7]; here we note simply that the current efficiency for the DC chromium was 16% and the current efficiency for the PR chromium was 28%. Thus, during the anodic pulse, Cr^{3+} ions are concentrated near to the electrode and inhibit deposition temporarily. Also, it is well known that hydrogen is codeposited during chromium deposition and some of the charge loss is due to this hydrogen deposition.

Concurrently with Cr deposition, H^+ is reduced and adsorbed on the cathode as atomic hydrogen (H ad-atoms). In later reaction steps, H_2 molecules are formed on the surface. By surface diffusion the molecules then join with other molecules until a critical bubble size has been reached; the bubble then escapes from the surface as H_2 gas. During the deposition of the PR Cr, the anodic period is 0.3 s where some of the H ad-atoms are re-oxidized and dissolved into the solution: $H(ad) \rightarrow H^+(aq) + e^-$. It is difficult to estimate the amount of re-oxidized hydrogen, since a parallel redissolution of chromium also takes place [24]. Likewise, it is difficult to estimate the difference in the concentration of H ad-atoms during deposition of DC and PR chromium, respectively. However, from the pulse pattern experiments performed [7], the PR chromium that showed the highest current efficiency was the one that has been presented here. This suggests that the conditions were such that nearly all H ad-atoms were pulled back into the electroplating solution. It was also shown that the optimum charge in the anodic pulse, considering the current efficiency, was a function of the charge passed in the previous cathodic pulse. The higher the cathodic charge, the higher the anodic charge is needed to reach the optimum current efficiency. The optimum anodic charge was found to be typically of the order of 1% of the cathodic charge. It may be concluded that the electrodeposition of DC chromium is therefore associated with a higher concentration of H ad-atoms than the PR chromium.

4.2. *Crystal orientation*

From the X-ray experiment it has been established that the DC Cr is highly <2 2 2> textured and that the PR Cr has a random distribution of crystal directions. It is not reasonable to state that the DC Cr texture is a result of an outwards growth mode, because of a high current density and a low electrodeposition temperature, since the PR Cr, without this texture, has exactly the same cathodic plating parameters in the cathodic period. Moreover, PR Cr has a random crystal distribution [17, 18] suggesting that very little inhibition has taken place during the deposition of PR Cr.

4.3. *Grain size*

The grain size of the deposits has been evaluated in three ways: X-ray diffraction, hardness measurements and XTEM. The hardness and X-ray diffraction results are in agreement, namely, that the grains of the DC Cr are much smaller than the grains of the PR Cr, at least within a factor of three. According to Fischer [25] the growth of columnar crystals is a result of inhibition of lateral growth. Hence, the smaller the grains, the larger the effect of morphological inhibition. The grain size of the electrodeposits therefore indicates also that there has been a larger inhibition of the DC Cr than the PR Cr.

4.4. *Microcracks*

In Figs 5 and 6 it can be seen that the DC Cr has a high microcrack density and that the PR Cr has a zero crack density. According to Weil [26] a possible source of residual tensile stresses in electrodeposits can be understood as result of grains accommodating boundary misfit at grain coalescence. This idea is also used to explain residual stresses in coatings made by vacuum deposition methods [27]. The higher the inhibition of lateral grain growth, the higher the nucleation rate and so the higher number of grains that coalesce thereby leading to higher residual tensile stresses. This leads to the conclusion that the higher the residual tensile stresses the higher the inhibition of the growth has been. Therefore, the presence of microcracks in the DC Cr and not in the PR Cr may also be interpreted to support the suggestion of a higher inhibition of grain growth in the DC Cr than in the PR Cr.

4.5. *Precipitates and microstructure of the DC Cr*

The presence of chromium oxide in the microstructure of a <1 1 1> textured electrodeposited chromium has been investigated using cross-sectional transmission electron microscopy and X-ray diffraction. It has been found that Cr_2O_3 is codeposited on the {1 1 1} planes of the chromium and that Cr_2O_3 is present at up to 5 vol % of the coating. Similar chromium oxides were not found in the PR chromium. The presence of Cr oxides in the DC Cr and the lack of the same Cr oxides in the PR Cr substantiates the argument that there is a higher concentration of H ad-atoms on the surface of the DC Cr than on the PR Cr. According to the Pourbaix diagram (that shows the thermodynamically stable phases of Cr and Cr derivates in the terms of the pH value and the voltage, E) Cr_2O_3 can become stable if the pH value is higher than for normal Cr electrodeposition. Thus, if more H^+ ions are reduced on the DC Cr than on the PR Cr growth front, the pH value will rise more on the DC Cr cathode than on the PR Cr cathode. This will, in some places, even lead to codeposition of Cr_2O_3 on the DC Cr growth front. The above argumentation is supported by the fact that the current efficiency of the DC Cr deposition is lower than the current efficiency of the PR Cr deposition. Following the above argumentation, then since the H ad-atom concentration is higher in the deposition of DC Cr than in the deposition of the PR Cr and since the microstructure of the DC Cr shows evidence of inhibited growth, then it is likely that it is the H^0 atoms that are the major inhibiting species.

4.6. *Inhibiting species*

It is well known that conventional electrodeposition of DC chromium is associated with the codeposition of large amounts of hydrogen. It has been shown that at low temperatures a hexagonal close packed CrH and face centred cubic CrH_2 can be plated [5, 6, 9]. It is, therefore, clear that, under some circumstances, hydrogen is codeposited and may even be incorporated in the chromium. It has been suggested, as for nickel electrodeposition, that an inhibiting specie is simply adsorbed hydrogen [19, 28] and is likely also for chromium deposition. The higher the $\{h\,k\,l\}$ index of a crystal facet, the more chemically active the crystal face will be, and hence the more hydrogen will be adsorbed. This explains why a hydrogen saturated surface only develops the lowest index crystal face, which is the {1 1 1} face, (presented as a {2 2 2} peak in the diffraction pattern in Fig. 1.

5. Conclusion

The microstructure of a direct current (DC) electrodeposited chromium and a pulse reversed (PR) electrodeposited chromium have been investigated using X-ray diffraction and cross-sectional transmission electron microscopy.

The DC Cr is strongly <1 1 1> textured, has small grains and there occurs codeposition of Cr_2O_3 nanoparticles. The PR Cr has an almost random distribution of crystal orientations. The PR Cr has larger grains than the DC Cr and there are no codeposited nanoparticles of Cr_2O_3.

Since the current efficiency of PR Cr is 75% higher than that of the DC CR it is suggested that more hydrogen is reduced on the DC Cr growth front and that this H concentration leads to inhibition of crystal nuclei other than the nuclei having a <1 1 1> direction. The presence of Cr_2O_3 nanoparticles supports the idea that more H^+ ions are reduced on the DC cathode than on the PR cathode since the reduction of H^+ to H^0 will increase the pH value making the Cr_2O_3 phase thermodynamically stable. All the above observations are found to be consistent with hydrogen inhibition and its effect on texture formation.

Acknowledgements

We wish to thank Jørgen Lindbo and Knud Jensen for technical assistance. The present work is part of an ongoing programme of coatings and layered structures within the Engineering Science Centre at Risø National Laboratory.

References

[1] O. Berkh, S. Eskin and J. Zahavi, *Plat. Surf. Finish.* **83**(3) (1994) 62.

[2] A. R. Jones, *ibid.* **76**(4) (1989) 62.

[3] T. Pearson and K. Dennis. *ibid.* **76**(11) (1989) 64.

[4] J. P. Hoare, *ibid.* **76**(9) (1989).

[5] J-H. Chai, D-Y. Chang and S.-C. Kwon, *ibid.* **76**(6) (1989) 80.

[6] R-Y. Tsai and S-T. Wu. *J. Electrochem. Soc.* **137** (1990) 3057.

[7] P. Leisner. PhD thesis, The Technical University of Denmark (1992).

[8] C. Bergenstof Nielsen *et al.*, Extended Abstracts of 45th Scandinavian Society for Electron Microscopy, Scandem, June (1993) 135.

[9] C. A. Snavely, *Trans. Electrochem. Soc.* **92** (1948) 537.

[10] M. R. Wyllie, *J. Chem. Phys.* **16** (1948) 52.

[11] R. M. Bozorth, *Phys. Rev.* **26** (1925) 390.

[12] H. Wilman, *Trans. Inst. Metal. Finish.* **32** (1955) 281.

[13] St. Rashkov, D. S. Stoichev and I. Tomov, *Electrochim. Acta* **17** (1972) 1955.

[14] G. I. Finch, A. G. Quarrel and H. Wilman, *Trans. Faraday Soc.* **31** (1935) 1051.

[15] G. I. Finch, *Z. Elektrochem.* **54** (1950) 457.

[16] N. A. Pangarov, *J. Electroanal. Chem.* **9** (1965) 70.

[17] S. Toschev, M. Pannov and R. Kaischew, *Izv. Otd. Khim. Nauki.* **1** (1968) 119.

[18] J. Thevenin, *J. Microsc. Spectr. Electron.* **1** (1976) 7.

[19] J. Amblard, I. Epelboin, M. Froment and G. Maurin, *J. Appl. Electrochem.* **9** (1979) 233.

[20] E. O. Hall, *Proc. Phys. Soc.* (*London*). **B64** (1951) 747.

[21] J. Lindbo and T. Leffers, *Metallography* **5** (1972) 473.

[22] C. Tang, S. Alexander and R. Bruinsma, *Phys. Rev. Lett.* **64** (1990) 772.

[23] A. L. Barabási and H. E. Stanley, 'Fractal Concepts in Surface Growth', Cambridge University Press, Cambridge (1995).

[24] P. Leisner, G. Bech-Nielsen and P. Møller, *J. Appl. Electrochem*, **23** (1993) 1232.

[25] H. Fischer, *Electrodepos. Surf. Treat.* **1** (1972/73) 319.

[26] R. Weil, *Annu. Rev. Mater Sci.* **19** (1989) 165.

[27] R. Koch, *J. Phys. Condens. Matter* **6** (1994) 9519.

[28] A. K. N. Reddy, *J. Electroanal. Chem.* **6** (1963) 141.